The Astrophysical Journal, 965:52 (11pp), 2024 April 10 https://doi.org/10.3847/1538-4357/ad276a

Unraveling the Cr Isotopes of Ryugu: An Accurate Aqueous Alteration Age and the Least Thermally Processed Solar System Material

Ryoji Tanaka[1], Dilan M. Ratnayake[1], Tsutomu Ota[1], Noah Miklusicak[1], Tak Kunihiro[1], Christian Potiszil[1], Chie Sakaguchi[1], Katsura Kobayashi[1], Hiroshi Kitagawa[1], Masahiro Yamanaka[1], Masanao Abe[2,3], Akiko Miyazaki[2], Aiko Nakato[2], Satoru Nakazawa[2], Masahiro Nishimura[2], Tatsuaki Okada[2,4], Takanao Saiki[2], Satoshi Tanaka[2,3], Fuyuto Terui[2,5], Yuichi Tsuda[2,3], Tomohiro Usui[2], Sei-ichiro Watanabe[6], Toru Yada[2], Kasumi Yogata[2], Makoto Yoshikawa[2,3], and Eizo Nakamura[1]

[1] The Pheasant Memorial Laboratory for Geochemistry and Cosmochemistry, Institute for Planetary Materials, Okayama University, Yamada 827, Misasa, Tottori 682-0193, Japan; ryoji@okayama-u.ac.jp
[2] Institute of Space and Astronautical Science, Japan Aerospace Exploration Agency, Sagamihara, 252-5210, Japan
[3] Department of Space and Astronautical Science, The Graduate University for Advanced Studies, Hayama, 240-0193, Japan
[4] Graduate School of Science, The University of Tokyo, Tokyo, 113-0033, Japan
[5] Department of Mechanical Engineering, Kanagawa Institute of Technology, Atsugi, 243-0292, Japan
[6] Department of Earth and Planetary Sciences, Nagoya University, Nagoya 464-8601, Japan
Received 2023 December 29; revised 2024 February 2; accepted 2024 February 6; published 2024 April 4

Abstract

The analysis of samples returned from the C-type asteroid Ryugu has drastically advanced our knowledge of the evolution of early solar system materials. However, no consensus has been obtained on the chronological data, which is important for understanding the evolution of the asteroid Ryugu. Here, the aqueous alteration age of Ryugu particles was determined by the Mn–Cr method using bulk samples, yielding an age of $4.13 + 0.62/-0.55$ Myr after the formation of Ca–Al-rich inclusions (CAI). The age corresponds to $4563.17 + 0.60/-0.67$ Myr ago. The higher $^{55}Mn/^{52}Cr$, $\varepsilon^{54}Cr$, and initial $\varepsilon^{53}Cr$ values of the Ryugu samples relative to any carbonaceous chondrite samples implies that its progenitor body formed from the least thermally processed precursors in the outermost region of the protoplanetary disk. Despite accreting at different distances from the Sun, the hydrous asteroids (Ryugu and the parent bodies of CI, CM, CR, and ungrouped C2 meteorites) underwent aqueous alteration during a period of limited duration (3.8 ± 1.8 Myr after CAI). These ages are identical to the crystallization age of the carbonaceous achondirtes NWA 6704/6693 within the error. The $\varepsilon^{54}Cr$ and initial $\varepsilon^{53}Cr$ values of Ryugu and NWA 6704/6693 are also identical, while they show distinct $\Delta'^{17}O$ values. This suggests that the precursors that formed the progenitor bodies of Ryugu and NWA 6703/6693 were formed in close proximity and experienced a similar degree of thermal processing in the protosolar nebula. However, the progenitor body of Ryugu was formed by a higher ice/dust ratio, than NWA6703/6693, in the outer region of the protoplanetary disk.

Unified Astronomy Thesaurus concepts: Asteroids (72); Carbonaceous chondrites (200)

1. Introduction

The asteroid Ryugu, observed and sampled by JAXA's Hayabusa2 spacecraft, is a C-type asteroid for which comprehensive physical, geological, petrological, and chemical data are available (Sugita et al. 2019; Watanabe et al. 2019; Yada et al. 2021; Ito et al. 2022; Nakamura et al. 2022; Tachibana et al. 2022; Yokoyama et al. 2023a; Nakamura et al. 2023). The asteroid Ryugu has a spinning-top shape with an equatorial radius of 502 m, a bulk density of $1190 \pm 20\,kg\,m^{-3}$, and a rubble pile structure with high porosity (~50%) (Sugita et al. 2019; Watanabe et al. 2019). The Ryugu samples consist of phyllosilicates (serpentine and saponite) as their main constituent minerals, with minor amounts of carbonate, magnetite, Fe-sulfide, and organic matter (Ito et al. 2022; E. Nakamura et al. 2022; T. Nakamura et al. 2023). The samples were less affected by thermal processes in the protoplanetary disk compared to the carbonaceous chondrites obtained so far, and contain the most pristine materials in the protoplanetary disk (Ito et al. 2022; Nakamura et al. 2022; Yokoyama et al. 2023a; Nakamura et al. 2023). Therefore, accurate chronological data of the progenitor body of the asteroid Ryugu is an important parameter for understanding the evolution of planetesimals in the outer protoplanetary disk.

The ^{53}Mn–^{53}Cr system, the short-lived nuclide ^{53}Mn that decays to ^{53}Cr with a half-life of 3.7 Myr (Honda & Imamura 1971), has been used as a suitable tool for determining the aqueous alteration age of chondrites (Endress et al. 1996). Three papers so far have reported aqueous alteration ages for the Ryugu progenitor body, via the Mn–Cr method for carbonates using secondary ion mass spectrometry (SIMS; Nakamura et al. 2022; Yokoyama et al. 2023a; McCain et al. 2023) (Figure 1). However, these three papers reported different values of 5.2, 2.6, and 0.0–0.5 Myr after the formation of Ca–Al-rich inclusions (CAI) using an initial $(^{53}Mn/^{55}Mn)_0$ value and the U-corrected Pb–Pb age in D'Orbigny (Brennecka & Wadhwa 2012) and the U-corrected Pb–Pb age of CAI (Connelly et al. 2012) (Figure 1). Each study analyzed samples collected at two different touchdown (TD) sites (TD1 and TD2), and the Mn–Cr ages obtained at both sites were nearly identical. Therefore, the cause of the different ages reported does not result from variable alteration ages, but rather as a result of the different matrix effect correction procedures used for SIMS analysis (McCain et al. 2023). Whether the age of

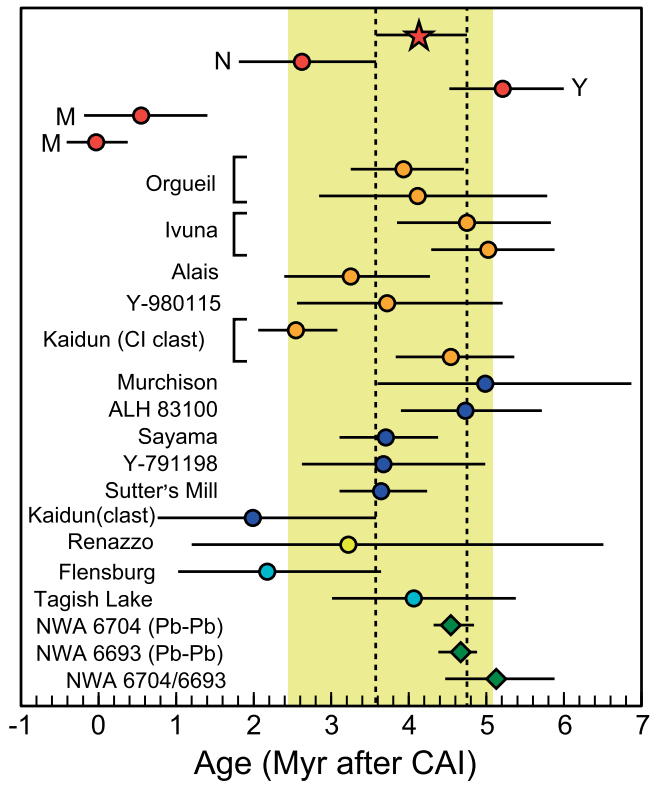

Figure 1. The compiled Mn–Cr ages of Ryugu. The data obtained in this study (red star) and those previously reported (red circle: N (Nakamura et al. 2022), Y (Yokoyama et al. 2023a), and M (McCain et al. 2023). For comparison, the Mn–Cr ages of Type 1 and 2 carbonaceous chondrites (CI (orange circle)), CM (blue circle), CR (yellow circle), and C2-ungrouped (light-blue circle)) (Petitat et al. 2011; Fujiya et al. 2012, 2013; Jilly-Rehak et al. 2017; Visser et al. 2020; Bischoff et al. 2021), and the Mn–Cr and Pb–Pb age of NWA 6704/6693 (green diamond; Sanborn et al. 2019) are also plotted (see the details in the main text). The ages are expressed as after the formation of CAI (4567.30 Myr ago, Connelly et al. 2012). Yellow zones represent mean ±2SD ranges for CI, CV, CR, and C2-ungrouped chondrites (3.8 ± 1.8 Myr). Even if the age data of Ryugu measured in this study was included in the calculation for the mean value, the mean, and 2SD values are identical. The broken line shows the 2SE range of Mn–Cr age values for the Ryugu particles obtained in this study. All the age data were calculated using the initial $(^{53}Mn/^{55}Mn)_0$ value and the U-corrected Pb–Pb age of D 'Orbigny ($3.24 \pm 0.04 \times 10^{-6}$ and 4563.37 ± 0.25 Myr ago; Brennecka & Wadhwa 2012) and the U-corrected Pb–Pb age of CAI (4567.30 ± 0.16 Myr ago; Connelly et al. 2012).

aqueous alteration was <1 or >5 Myr after CAI formation has major implications in estimating the age of accretion, the size, and the thermal history of the Ryugu progenitor body. Therefore, it is important to accurately determine the aqueous alteration age of the Ryugu samples.

Thermal ionization or inductively coupled-plasma mass spectrometry (TIMS and ICP-MS, respectively) measurements using bulk samples with the appropriate pretreatment gave highly accurate and precise Mn/Cr and Cr isotopic data that were independent of the matrix composition (Birck & Allègre 1985). The accuracy of the Mn–Cr dating method using TIMS/ICP-MS was confirmed by the determination of concordant crystallization ages for achondrites using other techniques such as the Pb–Pb and Mg–Al methods (Amelin et al. 2019; Sanborn et al. 2019). However, it was hard to determine the Mn–Cr ages for carbonaceous chondrites using the bulk samples because they were not fully equilibrated by the asteroidal processes that affected them.

The Hayabusa2 Phase-2 curation facility at the Pheasant Memorial Laboratory (P2C-PML) reported comprehensive petrological and cosmochemical data for 16 representative Ryugu particles (Nakamura et al. 2022). The majority (>99% for all samples except for one sample with 97%) of minerals in these Ryugu particles were formed as a result of aqueous alteration. Among the samples from both TD sites, the TD2 particles show relatively homogeneous chemical compositions. On the other hand, the TD1 samples show significant heterogeneity especially for the refractory lithophile elements, suggesting that elemental fractionation beyond the sample size may have occurred due to aqueous alteration. The modal abundance of carbonates, the main reservoir of Mn, also varied significantly among the Ryugu particles (0.4–6.9 vol.%) and was particularly pronounced among the TD1 particles.

The oxygen isotope compositions of five representative samples measured at the P2C-PML gave a mass-dependent relationship with a wide range of $\delta^{18}O$ values ($^{18}O/^{16}O$ relative to the Vienna Standard Mean Ocean Water) between 17.7 and 20.1‰ (Nakamura et al. 2022). Such an observation indicates that aqueous alteration achieved oxygen isotope equilibrium at least on the scale of a given particle. The $\Delta'^{17}O$ value (definition is shown in the footnote of Table 1) of all Ryugu samples measured so far (except C0002), including the five samples measured by Nakamura et al. (2022), were identical within the analytical uncertainty (Greenwood et al. 2022; Ito et al. 2022; Yokoyama et al. 2023a). This suggests that even oxygen, which generally diffuses slower than Mn and Cr in silicate minerals (e.g., Spandler & O'Neill 2010), reached isotopic equilibrium among most of the Ryugu samples. However, some samples, such as C0002, contain less altered fragments, and one of the fragments in C0002 contains up to 26 vol.% of anhydrous silicate minerals (olivine and pyroxene) (Nakamura et al. 2023). The $\Delta'^{17}O$ values of anhydrous silicates in the Ryugu samples range from 0 to −51‰ (Kawasaki et al. 2022; Liu et al. 2022; Nakamura et al. 2022), suggesting that the low $\Delta'^{17}O$ values of C0002 (Yokoyama et al. 2023a) could be due to the existence of these unequilibrated phases. Therefore, since the presence of such nonequilibrium phases can disturb the Mn–Cr system, it is necessary to evaluate whether the Mn–Cr system of the samples was equilibrated to obtain accurate chronological data.

In this study, the accurate aqueous alteration age of the Ryugu progenitor body will be determined via Mn–Cr chronology using the bulk particles. Chromium isotopes can also provide insight into the origin of the dust components that formed the planetesimals of the solar system. Furthermore, information concerning the location of planetesimal accretion can also be obtained, through the measurement of nucleosynthetic ^{54}Cr anomalies and the initial $^{53}Cr/^{52}Cr$ ratio. Therefore, the aqueous alteration age of Ryugu and the origin of its progenitor planetesimal's dust component and its accretion location will be discussed in this study.

2. Samples and Analytical Methods

The samples measured in this study were selected from the Ryugu particles distributed to the P2C-PML for the initial sample analysis of JAXA's Hayabusa2 mission. After the initial analyses (Nakamura et al. 2022; Potiszil et al. 2023), in which two particles were analyzed for Cr isotopes, there remained seven samples that possessed enough mass to allow Cr isotope analysis by the current study. Five particles

Table 1
Mn–Cr Data for Ryugu and Carbonaceous Chondrites

Sample[a]	Weight[b]	$^{55}Mn/^{52}Cr$[c]	$\varepsilon^{53}Cr$	2SE	$\varepsilon^{54}Cr$	2SE	N	Blank (%)	$\Delta'^{17}O$[d]
Ryugu particles									
A0022	0.444	3.780	1.19	0.12	1.37	0.18	8	<0.1	0.506
A0033	0.367	2.774	0.90	0.07	1.90	0.16	10	0.8	0.503
A0048	0.297	0.601	0.36	0.10	1.44	0.29	9	1.0	⋯
C0008	0.516	1.183	0.50	0.17	1.74	0.15	9	0.7	0.503
C0019	0.473	1.159	0.50	0.10	1.86	0.22	9	0.9	0.615
C0027	0.423	0.770	1.27	0.09	1.47	0.32	10	0.7	⋯
C0047	0.192	0.532	0.32	0.13	1.49	0.14	6	1.1	⋯
C0053	0.386	0.758	0.35	0.06	1.47	0.14	10	0.5	⋯
C0081	0.457	0.736	0.26	0.10	1.52	0.11	8	<0.1	⋯
Carbonaceous chondrite									
Murchison	8.67	0.722	0.22	0.07	0.94	0.21		⋯	−2.905
(1)			0.19	0.11	0.97	0.19	23	<0.1	⋯
(2)			0.26	0.07	0.92	0.37	9	<0.1	
Allende	10.2	0.514	0.12	0.05	0.83	0.12		⋯	−3.604
(1)			0.10	0.08	0.91	0.18	10	<0.1	⋯
(2)			0.13	0.07	0.75	0.15	10	<0.1	⋯
Orgueil	1.23	0.849	0.27	0.08	1.42	0.08		⋯	0.327
(1)			0.24	0.15	1.45	0.14	10	<0.1	⋯
(2)			0.31	0.08	1.39	0.07	15	<0.1	⋯

Notes.
[a] (1) and (2) for chondrite samples indicate different Cr fractions separated by ion chromatography using a different aliquot of the same dissolved solution. The mean values of (1) and (2) are shown on the top lines for each chondrite. The aliquot numbers used for the analyses were A0022-16, A0033-22, A0048-14, C0008-24, C0019-11, C0027-12, C0047-8, C0053-9, and C0081-5.
[b] Dissolved sample weight in milligrams.
[c] Analytical precision is 0.5% based on multiple measurements ($N = 5$) of BHVO-2 solution.
[d] Data are from Nakamura et al. (2022). $\Delta'^{17}O$ is defined as $\ln(\delta^{17}O+1) - 0.528 \times \ln(\delta^{18}O+1)$, where $\delta^{17\text{ or }18}O = (^{17\text{ or }18}O/^{16}O_{sample})/(^{17\text{ or }18}O/^{16}O_{VSMOW}) - 1$.

contained 0.0–0.5 vol.% of anhydrous silicate minerals (Table 2), which were not affected by the aqueous alteration process. The anhydrous silicate minerals could be fragments of ameboid olivine aggregates and chondrules (Nakamura et al. 2022). However, contributions from the anhydrous silicate minerals did not significantly modify the oxygen isotope composition of the bulk particles, beyond the analytical error. In all the measured particles, chondrule-like and CAI-like objects (Nakamura et al. 2023; Nakashima et al. 2023) were not found.

The detailed method for the sample digestion, purification, and elemental and isotope analysis has been described elsewhere (Makishima et al. 2010; Nakamura et al. 2022; Ratnayake et al. 2023). Approximately 0.2–0.5 mg of samples were weighed in an Au boat, and then transferred to a 7 mL PFA vial. The samples were digested using distilled concentrated HF and HNO_3 (1:1) in an ultrasonic bath for ∼6 hr, followed by heating on a hot plate, where the plate-surface temperature was kept at 195°C for 4 days. The sample was then dried, dissolved in 6M HCl, dried, and further decomposed in aqua regia at 170 °C for 2 days. After evaporating, the samples were dissolved in 0.5 M HNO_3. An aliquot of solution was used for Mn/Cr analysis and the other aliquot for Cr isotope analysis.

For the measurement of the Mn/Cr, a ^{53}Cr-enriched spike prepared by Yamakawa et al. (2009) was added to the solution and heated at 120 °C and dried. After adding an adequate amount of 0.5 M HNO_3, the Mn/Cr was determined by an isotope-dilution-internal standardization method after Makishima et al. (2010) using a sector type ICP-MS (ELEMENT XR, Thermo Scientific, Germany). For the isotope analysis, Cr was purified from the matrix elements through three ion-exchange steps, each using the cation exchange resin (AG50W-X8, Bio-Rad Laboratories, USA, 200–400 mesh size). Recoveries of Cr were >90%. The Cr isotopes were determined by TIMS (TRITON Plus, Thermo Scientific, Germany) using a total evaporation-bracketing method (van Kooten et al. 2016). The detailed analytical procedures for the Cr isotope analyses and data reduction are reported in Ratnayake et al. (2023). Approximately 20–40 ng of Cr and a Nb–H_3PO_5 activator were loaded onto each filament, and six to 10 measurements, depending on the purified amount of Cr, were performed for each sample. The NIST SRM 979 Cr standard was bracketed for each unknown sample measurement. The data with ^{52}Cr >2V was used for the data reduction, and the interference and instrumental mass fractionation correction was performed for each scanned data. The $\varepsilon^{53}Cr$ and $\varepsilon^{54}Cr$ values were calculated relative to the NIST SMR 979, where $\varepsilon^{i}Cr = 10^4 \times [(^{i}Cr/^{52}Cr_{sample})/(^{i}Cr/^{52}Cr_{NIST\ SRM\ 979}) - 1]$ and $i = 53$ or 54).

The instrumental mass fractionation law was evaluated by calculating the slope between $\ln(^{52}Cr/^{50}Cr)$ and $\ln(^{53}Cr/^{50}Cr)$ for $^{53}Cr/^{52}Cr$ and between $\ln(^{52}Cr/^{50}Cr)$ and $\ln(^{54}Cr/^{50}Cr)$ for $^{54}Cr/^{52}Cr$ for all the obtained data. The obtained slopes were 0.4877 ± 0.0056 (2SD, $N = 435$, median 0.4873) and 0.9529 ± 0.0098 (2SD, $N = 435$, median 0.9536) for the former and latter, respectively. By comparing the theoretical fractionation laws (linear, power, exponential, Rayleigh, and equilibrium laws), the obtained slopes were most close to the exponential law (0.4871) for $^{53}Cr/^{52}Cr$ and in the middle of exponential (0.9642) and Rayleigh (0.9458) laws for $^{54}Cr/^{52}Cr$ as described previously (Ratnayake et al. 2023). The reason for the different fractionation laws between $^{53}Cr/^{52}Cr$ and $^{54}Cr/^{52}Cr$ may arise from the residual mass-dependent fractionation due to the evaporation of Cr-oxide species present during thermal ionization (Bourdon & Fitoussi 2020; Yokoyama et al. 2023b).

Table 2
Modal Abundance of Minerals, the Proportion of Mn and Cr in Each of the Mineral Phases, and the Corrected $^{55}Mn/^{52}Cr$ and $\varepsilon^{53}Cr$ Values

	A0022	A0033	A0048	C0008	C0019	C0027	C0047	C0053	C0081
Modal abundance (vol.%)[a]									
Phyllosilicate (matrix)	83.6	85.7	91.7	91.1	77.6	66.5	91.2	89.8	88.3
Phyllosilicate (nodule)	⋯	2.1	1.6	2.4	8.3	20.9	1.3	1.4	5.7
Carbonate	6.9	6.8	0.4	1.7	3.7	2.2	2.2	1.8	1.6
Magnetite	5.4	2.9	4.8	2.4	5.1	6.5	1.5	3.7	1.7
Fe-sulfide	3.5	2.0	1.2	1.4	4.0	2.5	2.5	1.7	1.1
Phosphate	0.5	0.5	0.3	0.7	0.8	1.1	0.6	1.0	0.9
Anhydrous silicates	⋯	⋯	⋯	0.3	0.0	⋯	0.3	0.4	0.5
Carbonaceous nodule	⋯	⋯	⋯	0.0	0.4	0.2	0.4	0.1	0.3
Cr–Mn–Fe-rich oxide	⋯	⋯	⋯		0.0800	0.0815	⋯	⋯	⋯
Al-rich spinel	⋯	⋯	⋯	0.0146	⋯	⋯	⋯	0.0390	0.0131
Cr-rich spinel	0.0274	0.0156	0.0114	⋯	⋯	⋯	0.0341	⋯	0.0480
Proportion of Mn (%)[b]									
Phyllosilicate	3.8	4.0	35.9	15.0	6.5	10.0	11.8	13.4	15.2
Carbonate	93.9	94.5	49.8	79.5	84.9	75.5	84.3	78.9	78.7
Magnetite	1.5	0.8	11.2	2.3	2.3	4.5	1.2	3.3	1.6
Fe-sulfide	0.3	0.2	0.8	0.4	0.5	0.5	0.6	0.5	0.3
Phosphate	0.5	0.4	2.1	2.3	1.3	2.7	1.5	3.2	3.0
Anhydrous silicates	⋯	⋯	⋯	0.5	0.0	⋯	0.4	0.7	0.8
Carbonaceous nodule	⋯	⋯	⋯	0.0	0.0	0.0	0.0	0.0	0.0
Cr–Mn–Fe-rich oxide	⋯	⋯	⋯	⋯	4.4	6.8	⋯	⋯	⋯
Al-rich spinel	⋯	⋯	⋯	0.0	⋯	⋯	⋯	0.0	0.0
Cr-rich spinel	0.1	0.0	0.2	⋯	⋯	⋯	0.2	⋯	0.3
Proportion of Cr (%)[b]									
Phyllosilicate	91.7	95.4	96.0	98.5	94.7	94.7	92.3	97.8	90.3
Carbonate	0.0	0.0	0.0	0.0	0.0	0.0	0.0	0.0	0.0
Magnetite	1.8	0.9	1.5	0.8	1.7	2.1	0.5	1.2	0.5
Fe-sulfide	1.0	0.6	0.3	0.4	1.1	0.7	0.6	0.5	0.3
Phosphate	0.0	0.0	0.0	0.0	0.0	0.1	0.0	0.1	0.0
Anhydrous silicates	⋯	⋯	⋯	0.3	0.0	⋯	0.3	0.4	0.4
Carbonaceous nodule	⋯	⋯	⋯	0.0	0.0	0.0	0.0	0.0	0.0
Cr–Mn–Fe-rich oxide	⋯	⋯	⋯	⋯	2.4	2.4	⋯	⋯	⋯
Al-rich spinel	⋯	⋯	⋯	0.0	⋯	⋯	⋯	0.0	0.0
Cr-rich spinel	5.5	3.1	2.2	⋯	⋯	⋯	6.3	⋯	8.5
Corrected values[c]									
$^{55}Mn/^{52}Cr$ in Cr-rich spinel	0.01	0.01	0.10	⋯	⋯	⋯	0.03	⋯	0.04
$^{55}Mn/^{52}Cr_{corr.}$	3.78	2.78	0.60	1.18	1.16	0.77	0.53	0.76	0.74
$\varepsilon^{53}Cr_{corr}$	1.32	0.96	0.39	0.50	0.50	1.27	0.40	0.35	0.37

Notes.
[a] After adding the modal abundances of Cr–Mn–Fe-rich oxide, Al-rich spinel, and Cr-rich spinel calculated using the data obtained by Nakamura et al. (2022), the modal abundance of all phases (Nakamura et al. 2022) were recalculated.
[b] Densities for major and minor phases were taken from Nakamura et al. (2022), and those for Cr-rich spinel, Al-rich spinel, and Cr–Mn–Fe-rich oxides were taken as 4.8, 3.6, and 5.2, respectively. The Mn and Cr contents of each phases are taken from Nakamura et al. (2023) and Nakato et al. (2022).
[c] The corrected values are calculated after omitting the Mn and Cr in the Cr-rich spinel (see details in the main text).

Despite these problems with Cr isotope analysis using TIMS, there were no systematic differences in the degree of instrumental mass fractionation between the standard and the sample. Hence, the value corrected by the exponential law was used as the $^{53}Cr/^{52}Cr$ value, and the average of the values corrected by the Rayleigh and exponential laws was used for the $^{54}Cr/^{52}Cr$ value in accordance with the actual fractionation phenomena. In our previous study (Nakamura et al. 2022), the $^{54}Cr/^{52}Cr$ values were corrected by the exponential law. Thus, the published $\varepsilon^{54}Cr$ value for A0022 and C0081 (Nakamura et al. 2022) were recalculated.

The $\varepsilon^{53}Cr$ and $\varepsilon^{54}Cr$ values for the geological reference materials gave 0.02 ± 0.12 and -0.18 ± 0.19, respectively for PCC1 ($N = 18$) and 0.05 ± 0.09 and 0.05 ± 0.15, respectively, for JP1 ($N = 16$). The total procedural blank was <0.2 ng when C0081 and A0022 were measured, but was <2 ng when other samples were measured. This difference was attributed to the different batches of reagent (HCl) used during ion exchange. The Cr blank in the samples was <1%, but a blank correction was applied to the values obtained. The blank correction resulted in differences of up to 0.007 in $\varepsilon^{53}Cr$ values and 0.017 in $\varepsilon^{54}Cr$ values from the non-corrected values, and these differences were sufficiently small compared to the analytical error.

The ^{53}Cr and ^{54}Cr may be formed by spallation reactions with energetic particles in the early solar system (Shukolyukov & Lugmair 2006). However, due to the low Fe content in the

Table 3
Isotope Ratios of the Matrix (n = 10), Cr–Mn–Fe-rich Oxide (n = 27), and Dense Phyllosilicate Nodules (n =7) from All Target Areas in C0027 Measured by SIMS

Point #	Object	Diameter	ε^{53}Cr	2SE
8187-9	Matrix	12 μm	−6	16
8191-7	Matrix	10 μm	11	24
8197-3	Matrix	10 μm	−12	75
8198-4	Matrix	13 μm	−2	28
8200-5	Matrix	10 μm	55	78
8201-4[a]	Matrix	17 μm	−39	17
8204-3	Matrix	16 μm	−4	46
8205-7	Matrix	10 μm	−16	37
8208-3	Matrix	14 μm	−34	70
8209-4	Matrix	19 μm	−10	25
8187-1	Cr-rich oxide	3 μm	83	70
8187-2	Cr-rich oxide	3 μm	55	54
8187-3	Cr-rich oxide	4 μm	17	34
8187-4	Cr-rich oxide	4 μm	−18	51
8187-5	Cr-rich oxide	3 μm	−12	57
8187-6	Cr-rich oxide	3 μm	−8	55
8187-7	Cr-rich oxide	3 μm	66	55
8191-1	Cr-rich oxide	2 μm	29	38
8191-2	Cr-rich oxide	2 μm	−20	38
8191-3	Cr-rich oxide	2 μm	15	66
8191-4	Cr-rich oxide	2 μm	−8	48
8197-1	Cr-rich oxide	3 μm	−56	124
8197-2	Cr-rich oxide	2 μm	−124	239
8198-1	Cr-rich oxide	3 μm	9	75
8200-1	Cr-rich oxide	3 μm	−23	59
8200-2	Cr-rich oxide	2 μm	58	84
8200-3	Cr-rich oxide	2 μm	72	139
8201-1[a]	Cr-rich oxide	3 μm	63	16
8204-1	Cr-rich oxide	2 μm	−88	182
8204-2	Cr-rich oxide	3 μm	−42	193
8205-1	Cr-rich oxide	3 μm	−15	45
8205-3	Cr-rich oxide	3 μm	−49	70
8207-1	Cr-rich oxide	5 μm	−18	110
8207-2	Cr-rich oxide	4 μm	−25	151
8207-3	Cr-rich oxide	4 μm	−15	167
8208-1	Cr-rich oxide	3 μm	83	48
8209-1	Cr-rich oxide	3 μm	21	34
8187-8	Dense phyllosilicate nodule	10 μm	−15	22
8191-5	Dense phyllosilicate nodule	6 μm	−21	26
8191-6	Dense phyllosilicate nodule	3 μm	26	50
8198-3	Dense phyllosilicate nodule	5 μm	−22	46
8200-4	Dense phyllosilicate nodule	4 μm	79	69
8205-5	Dense phyllosilicate nodule	6 μm	52	44
8205-6	Dense phyllosilicate nodule	7 μm	−33	40

Note.
[a] The measure points shown in Figure 4(c).

Ryugu and carbonaceous chondrite samples, the correction was not necessary as described elsewhere (Shukolyukov & Lugmair 2006). Thus, no correction for spallation-related processes was performed.

In situ isotope ratio of $^{53}Cr/^{52}Cr$ in particle C0027 were determined by SIMS (ims-1280, Cameca, France). An aliquot of the sample was mounted in indium, and its surface was polished by ultra-microtome prior to coating with 750 nm of Au (Nakamura et al. 2022). The sample was irradiated by a $^{16}O^-$ primary beam of 23 keV over a scanning area of 25 × 25 μm^2. The primary beam current was 1 nA during pre-sputtering (120 s) and 100 pA during analysis. The mass resolution was set to 7500 to exclude the contribution of interference by $^{52}CrH^+$. A contrast aperture of 400 μm and a field aperture of 3000 μm were used, and an energy bandpass from −10 to 40 eV was set. Secondary ions ($^{52}Cr^+$, $^{53}Cr^+$, and $^{55}Mn^+$) were accelerated to −10 kV and collected by an axial electron multiplier in imaging mode. A typical total acquisition time was 10 hr. The isotope ratio was calculated so the mean value of all objects equals the bulk value of C0027. Matrix effects among phases were not considered. The analytical precision of $^{53}Cr/^{52}Cr$, 2SD external precision of repeated measurements of reference material (Cr spinel in KLB-1 peridotite) was ±84ε.

3. Results

The $^{55}Mn/^{52}Cr$ ratios of the nine Ryugu samples reported here have a range of 0.60–3.78 (Table 1), which is wider than that reported for other Ryugu samples (0.67–1.51, Yokoyama et al. 2023c) and for carbonaceous chondrites (0.31–0.85, Zhu et al. 2021). The mean of all $^{55}Mn/^{52}Cr$ values obtained in the P2C-PML (this study and Nakamura et al. 2022) is 1.2 ± 0.4 (2SE, N = 20), which is nearly identical to that measured by other Ryugu samples using 1–2 orders of magnitude larger mass of homogenized sample powders (1.1 ± 0.3, 2SE, N = 5, Yokoyama et al. 2023a, 2023c). The mean of all data (1.14 ± 0.30, 2SE, N = 25) is defined as the bulk Ryugu value. On comparing the mean ± 2SE value, two and five samples analyzed in this study show a $^{55}Mn/^{52}Cr$ excess and deficit, respectively (Figure 2). The $^{55}Mn/^{52}Cr$ and ε^{53}Cr of Ryugu particles, except for C0027, demonstrated a positive correlation (Figure 2). When considered as an isochron, $(^{53}Mn/^{55}Mn)_0$ and $\varepsilon^{53}Cr_0$ corresponded to (3.12 ± 0.34) ×10^{-6} and 0.147 ± 0.054, respectively, with the mean square weighted deviation (MSWD) = 0.81 (Figure 2). Using the initial $(^{53}Mn/^{55}Mn)_0$ value and the U-corrected Pb–Pb age of D'Orbigny (3.24 ± 0.04 × 10^{-6} and 4563.37 ± 0.25 Myr ago, Brennecka & Wadhwa 2012), the U-corrected Pb–Pb age of CAI (4567.30 ± 0.16 Myr ago, Connelly et al. 2012), an age of 4.13 +0.62/−0.55 Myr after CAI formation was obtained, which corresponded to an absolute age of 4563.17 +0.60/−0.67 Myr ago. While this age is intermediate between 5.2 +0.8/-0.7 (Yokoyama et al. 2023a) and 2.6 +1.0/−0.8 Myr (Nakamura et al. 2022), it is distinctively younger than 0.5 +0.9/−0.8 and 0.0 ± 0.4 Myr (McCain et al. 2023) after the CAI (Figures 1 and 2).

The ε^{54}Cr values of Ryugu samples have a range of 1.4–1.9, with a mean value of 1.57 ± 0.13 (2SE)(Table 1). Six out of the nine samples showed relatively homogeneous ε^{54}Cr values of 1.5 ± 0.1, while the remaining three had higher values between 1.7 and 1.9 (Figure 3). The mean ε^{54}Cr value of Ryugu samples was similar to that of CI chondrites (1.5 ± 0.2), but the samples with the highest three ε^{54}Cr values were clearly higher than those of CI chondrites (Figure 3). The ε^{54}Cr values obtained in this study are within the range of that reported by Yokoyama et al. (2023a, 2023c; 1.22–2.22), which measured a sample mass that was 1–2 orders of magnitude larger than what we used. The mean of the ε^{54}Cr values for all of the Ryugu data (this study and Yokoyama et al. 2023a, 2023c) is calculated as 1.60 ± 0.15 (2SE).

Meanwhile, C0027 reported the highest ε^{53}Cr value of +1.27, despite possessing a relatively low $^{55}Mn/^{52}Cr$ value of 0.77. This suggests that C0027 contains different components and/or experienced distinct processes from the other particles.

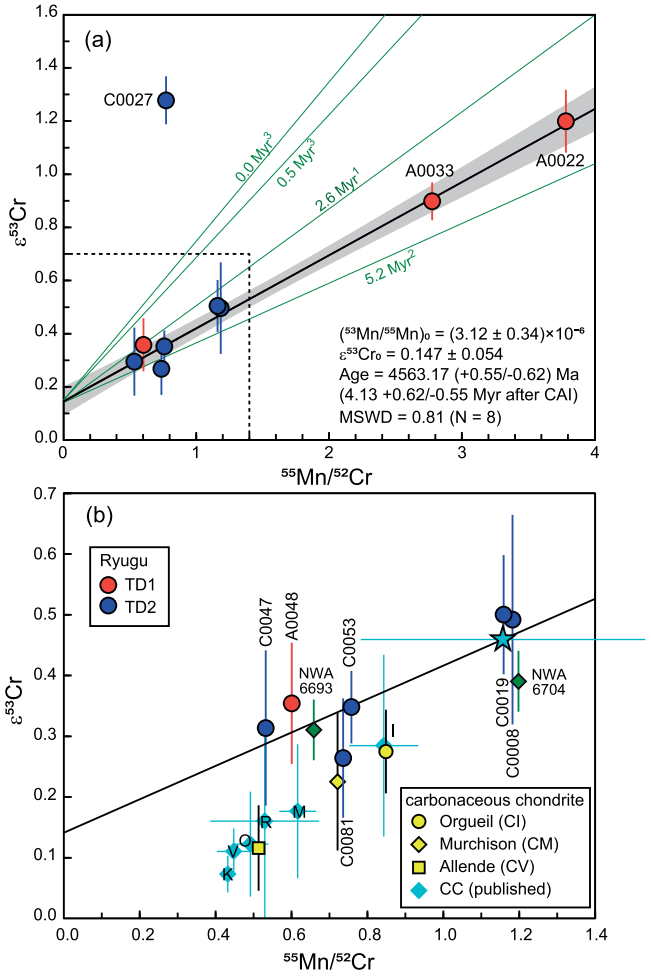

Figure 2. Plots of ^{55}Mn/^{52}Cr vs. ε^{53}Cr and isochrons for Ryugu particles. (b) represents a zoomed-in view of the area surrounded by the dashed line in (a). The Mn–Cr isochrons obtained from the carbonates measured by SIMS are given for reference (green lines): 1 Nakamura et al. (2022), 2 Yokoyama (2023a), 3 McCain et al. (2023). The carbonaceous chondrites measured in this study and the compiled average values of carbonaceous chondrites measured previously (Zhu et al. 2021) and NWA 6704/6693 (Sanborn et al. 2019) are also shown. The star represents the estimated bulk Ryugu value. I, M, R, O, V, and K are CI, CM, CR, CO, CV, and CK chondrites. The green diamonds represent the carbonaceous achondrite NWA 6704 and NWA 6693. The isochron was obtained by the linear regression model (model 1) of the IsoplotR software (Vermeesch 2018). The analytical precision of the ^{55}Mn/^{52}Cr values is smaller than the symbol size.

On the other hand, the ε^{54}Cr value of C0027 was not anomalous compared with the other samples. To examine the presence of an anomalous ε^{53}Cr component in C0027, in situ measurement of ε^{53}Cr values was performed by SIMS (Figure 4 and Table 3). The ε^{53}Cr values of the matrix, Cr-rich oxides, and phyllosilicate nodules were -6 ± 52 (2SD, $N = 10$), 2 ± 103 (2SD, $N = 27$), and 9 ± 86 (2SD, $N = 7$), respectively, indicating no significant difference in ε^{53}Cr values between these phases.

4. Discussion

4.1. Reliability of Mn–Cr Age

To obtain a reliable Mn–Cr age using bulk samples, the Mn–Cr system of the analyzed samples must have reached equilibrium at the time of aqueous alteration. The coefficient of variation of Mn of the Ryugu samples is about 3 times larger

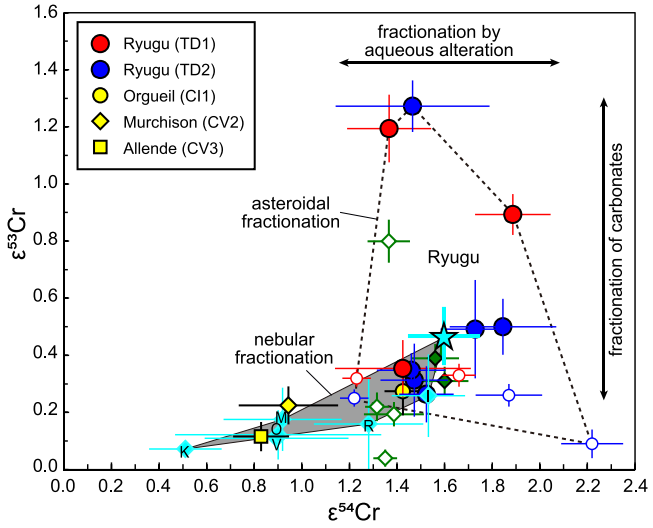

Figure 3. The relationship between ε^{53}Cr vs. ε^{54}Cr of the Ryugu samples. Data for the Cr isotopic compositions of carbonaceous chondrites (light-blue diamond, average with 2SE) are also included for comparison (Zhu et al. 2021). The anomalous data (Kadlag et al. 2019) in the compiled data (Zhu et al. 2021) was omitted. The ε^{54}Cr of the bulk Ryugu composition (light-blue star) is the average value of Ryugu samples (1.60 ± 0.15, 2SE) reported in this study and by Yokoyama et al. (2023c). Red and blue open circles represent Ryugu (TD1) and Ryugu (TD2) reported by Yokoyama et al. (2023c), green-filled diamonds represent NWA 6704/6693 (Sanborn et al. 2019), and green open diamonds represent other carbonaceous achondrites (NWA 7680, NWA 6962, Tafassasset, and NWA 011) (Bogdanovski & Lugmair 2004; Göpel et al. 2015; Sanborn et al. 2018; Hyde et al. 2022).

than that of Cr (2SD% = 64% for Mn and 20% for Cr, Nakamura et al. 2022). Therefore, the variation of ^{55}Mn/^{52}Cr depends mainly on the heterogeneity of Mn. To evaluate the contribution of Mn and Cr from each phase, a mass balance calculation was performed to estimate the proportions of Mn and Cr distributed in each mineral phase based on the modal abundance (this study and Nakamura et al. 2022) and the chemical compositions of each mineral (Nakato et al. 2022; Nakamura et al. 2023). The result indicated that 50–95% of the Mn in the Ryugu particles is contained within carbonates, with most of the rest being housed within phyllosilicates, magnetite, and phosphates (Table 2). In addition to these four mineral phases, sulfides and Cr–Mn–Fe oxides from the Ryugu samples were formed during aqueous alteration (Nakamura et al. 2022; Nakato et al. 2022), and Mn in the aforementioned minerals accounts for 99–100% of the bulk Mn. On the other hand, 90–99% of the Cr in the Ryugu samples is contained in phyllosilicates, and the total Cr distributed in the aqueously altered minerals accounts for 91–100% of the bulk Cr. Therefore, it is confirmed that the Mn/Cr of the Ryugu particles depends mainly on the modal abundance of carbonates (Figure 5). The heterogeneous ε^{54}Cr values among the Ryugu samples (Figure 3) could also be mainly caused by the fractionation of Cr due to the aqueous alteration process on the Ryugu progenitor body as discussed by Yokoyama et al. (2023c).

The Mg/Ca should also be controlled by the modal abundance of carbonate (Figure 5) for the reasons given below. The main reservoir of Mg in Ryugu particles is phyllosilicates, followed by carbonates, and of Ca is phyllosilicates and carbonates. Since most of the carbonates in the analyzed particles are dolomite, bulk Mg/Ca ratios of the Ryugu particles are dominantly controlled by the

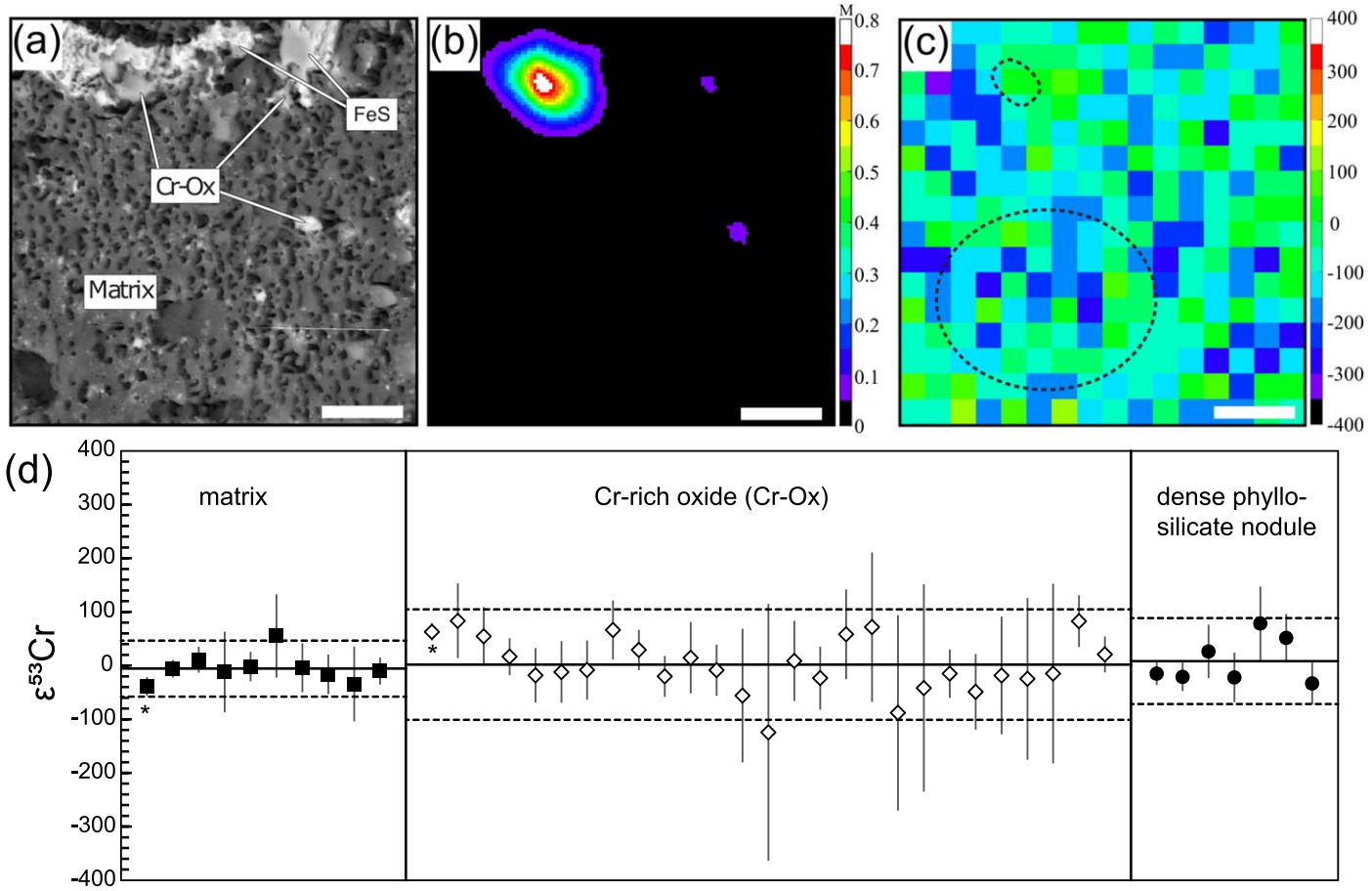

Figure 4. The occurrence of typical Cr-rich oxide grains in the matrix of C0027 and ε^{53}Cr of the matrix, Cr-rich oxides, and dense phyllosilicate nodules. (a) backscattered electron image of a target area with Cr-rich oxide (after SIMS analysis), (b) ion intensity map of $^{52}Cr^{+}$, and (c) isotope map of ε^{53}Cr. Isotope ratios ε^{53}Cr of the grains are indistinguishable from the surrounding matrix in (c) with a precision of ~84 representing 2SD of reproducibility observed on analyses on reference material (Cr spinel in KLB-1 peridotite). (d) Isotope ratios of the matrix, Cr-rich oxide, and dense phyllosilicate nodules from all target areas in C0027 (total = 6875 μm^2). The points marked with (*) correspond to the dotted areas in (c). Error bars are 2SE estimated from counting statistics. Solid and broken lines are average and 2SD of each domain.

phyllosilicates/dolomite ratio. Furthermore, of the other constituent minerals in Ryugu particles, magnetite, Fe-sulfides, phosphates, and Cr–Mn–Fe oxides, all but the phosphates have no effect on Mg/Ca. Only the abundance of phosphates affects bulk Ca content, but their modal abundance is <1% on average, so they do not significantly affect the bulk Mg/Ca. In fact, the Mn/Cr and Mg/Ca of the Ryugu particles follow along the mixing curve calculated by mass balance (Figure 5). The sample aliquots used for chemical analysis (Nakamura et al. 2022) and Mn/Cr and Cr isotopic analyses measured in this study were limited to <0.5 mg, respectively. Therefore, Mn/Cr heterogeneity associated with mineral heterogeneity between sample aliquots used in this and a previous study (Nakamura et al. 2022) was unavoidable. The Mn/Cr heterogeneity is particularly pronounced in samples with carbonate-rich particles (A0022 and A0033), and contrary, it was not observed for the carbonate-poor (0.43 vol.%) particle (A0048) (both are overlapping for A0048 in Figure 5). However, the heterogeneity was advantageous for the obtainment of the wide Mn/Cr variation observed in this study.

The TD1 particles were reported to display significant heterogeneity in their bulk chemical compositions, especially for P, Sr, and rare earth elements (REE), as a result of elemental fractionation due to aqueous alteration (Nakamura et al. 2022). Of the Ryugu samples measured in this study, A0022 and A0033 are enriched in the aforementioned elements, while A0048 is deficient in them (Nakamura et al. 2022). Mass balance calculations revealed that these elements migrated with the fluid, mainly as phosphate complexes during aqueous alteration, and they could have been precipitated as submicron-sized hydroxyapatite and amorphous phosphate compounds in the matrix (Nakamura et al. 2022). It is reasonable to assume that Mn, which has a higher solubility than Cr, was more likely to fractionate with these elements due to aqueous alteration. As the aqueous fluids contained CO_2 (E. Nakamura et al. 2022; T. Nakamura et al. 2023; Potiszil et al. 2023), the abundance of carbonates would also have been affected by aqueous alteration, resulting in their enrichment in A0022 and A0033 and depletion in A0048. On the other hand, the chemical heterogeneity among the TD2 particles, such as for P, Sr, and REE, is small. Furthermore, the variation in the modal abundances of carbonate among the TD2 particles was smaller than for the TD1 particles (Figure 5 and Table 2). In fact, no significant $^{55}Mn/^{52}Cr$ variations were observed among the TD2 particles.

During aqueous alteration, Al-rich spinel and Cr-rich spinel could have resisted alteration. Furthermore, five of the nine samples measured in this study (C0008, C0019, C0047, C0053, and C0081) contain 0–0.5 vol.% anhydrous silicates that were not affected by aqueous alteration. However, the proportions

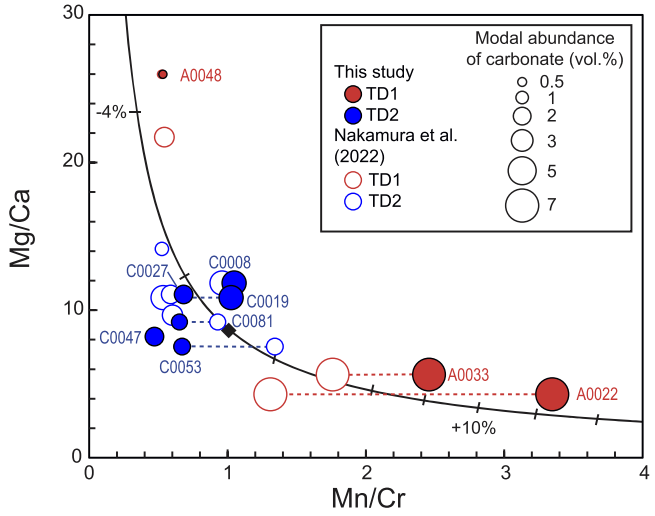

Figure 5. The Mn/Cr vs. Mg/Ca (mass ratio) of Ryugu particles. The size of the symbols indicates the modal abundance of the carbonate minerals in each particle after Nakamura et al. (2022). The Mn/Cr values were measured in both this and Nakamura et al. (2022) using different aliquots, and the same sample is connected by a broken line. The curve shows the calculated composition when dolomite is added to or subtracted from the average bulk composition of the Ryugu particles (tick marks = every 2%). The Mn/Cr and Mg/Ca of the bulk composition of Ryugu (solid diamond) used in the calculations were 1.01 (see the text for details) and 8.57 (average value of Nakamura et al. 2022 and Yokoyama et al. 2023a), respectively, the Mg/Ca and Mn concentration of dolomite were 0.568 and 3.90 wt.% (average value of Nakato et al. 2022; Nakamura et al. 2023), and Cr concentration of dolomite was zero.

of Mn and Cr in these anhydrous silicates were <0.8% and <0.4%, respectively, so the effect of these phases on the Mn–Cr system is negligible. The Mn and Cr contents of Al-rich spinel were lower than the detection limit for scanning electron microscopy with energy-dispersive X-ray spectroscopy; thus, the contributions of these elements in the Al-rich spinel could be negligible. On the other hand, Cr-rich spinel contains up to 8.5% of the bulk Cr. The $\Delta'^{17}O$ value of Cr-rich spinel in Ryugu particles is $-1.8 \pm 1.4‰$ (Kawasaki et al. 2022), which is lower than that of the bulk value revealing that isotopic equilibrium was not achieved during aqueous alteration. Therefore, the influence of Cr-rich spinel on the Mn–Cr system should be evaluated.

The mineralogical and cosmochemical signatures of the Ryugu particles most closely resemble those of CI chondrites (Ito et al. 2022; Nakamura et al. 2022; Yokoyama et al. 2023a). CI chondrites contain refractory phases with a wide range of $\varepsilon^{54}Cr$ and $\varepsilon^{53}Cr$ values. The highly acid-resistant phases in the CI chondrite Orgueil were found to be mainly composed of Cr-rich spinel and refractory silicates, which were characterized by a high $\varepsilon^{54}Cr$ (= +7.8 to +18.3) value and a low $\varepsilon^{53}Cr$ (= −0.84 to −0.93) and $^{55}Mn/^{52}Cr$ (= 0.10–0.14) values (Trinquier et al. 2008; Petitat et al. 2011). Thus, assuming that the $\varepsilon^{53}Cr$ value of Cr-rich spinel in Ryugu particles is the same as that of the highly acid-resistant phases in CI chondrites, the $^{55}Mn/^{52}Cr$ and $\varepsilon^{53}Cr$ values of the Ryugu data were corrected by omitting the contribution of Mn and Cr from the Cr-rich spinel (Table 2). These data gave $(^{53}Mn/^{55}Mn)_0 = (3.34 \pm 0.34) \times 10^{-6}$), $\varepsilon^{53}Cr_0 = 0.15 \pm 0.54$ (MSWD = 0.75). The Mn–Cr age obtained from this value was 3.77 +0.57/−0.52 Myr after CAI. While it is 0.36 Myr older than the uncorrected value, it is within the error range of the uncorrected value. Although mineralogical and chemical heterogeneity must have existed between the samples used for modal analysis and Mn–Cr analysis, due to the limited amount of sample used, this result indicates that the influence of the Cr-rich spinel on the Mn–Cr age value is likely within the analytical error. Therefore, the uncorrected Mn–Cr age is used as the aqueous alteration age of the Ryugu progenitor body in this study.

The Mn–Cr ages obtained by SIMS are highly dependent on the relative sensitivity factor (RSF) of Mn/Cr for the standard and the samples. Yokoyama et al. (2023a) and Nakamura et al. (2022) used a Ca-carbonate standard for the measurement of dolomite and pointed out the possibility of systematic errors due to the RSF values used. To eliminate this problem, McCain et al. (2023) prepared Cr-implanted dolomite as a standard and determined the Mn–Cr age of Ryugu carbonate as 0.4 ± 0.4 and 1.0 ± 0.8 Myr after the formation of CAI (0.0 and 0.5 Myr corrected by the same procedure used in this study). Our result is significantly different from that of McCain et al. (2023) and rather closer to those of the others (Nakamura et al. 2022; Yokoyama et al. 2023a). In order to validate the accuracy of the Mn–Cr age using SIMS, it is necessary to perform bulk and in situ analyses of the same carbonate minerals in a chondrite or Cr-implanted synthesized dolomite standards and compare the data from both. To achieve this, it is necessary to develop a high-precision bulk Cr isotope analysis method for ultra-trace amounts of Cr in the future.

4.2. Why Does C0027 Fall outside of the Isochron?

The possible processes that can enable a significant enrichment of the $\varepsilon^{53}Cr$ value in C0027 or its low $^{55}Mn/^{52}Cr$, relative to the isochron, could be (1) the presence of an abnormally high ^{53}Cr component within the dust that formed the Ryugu progenitor body or (2) the occurrence of two or more temporally isolated stages of Mn/Cr fractionation during aqueous alteration.

If we assume that the elevated bulk $\varepsilon^{53}Cr$ value of C0027 was caused by a Cr-rich oxide enriched in ^{53}Cr, then the mass balance calculation gave the $\varepsilon^{53}Cr$ value of the Cr-rich oxide as >40. However, the $\varepsilon^{53}Cr$ values of the Cr-rich oxide did not show significant variability and a spatial scale of 1 μm (Figures 4(c) and (d)). Even considering the influence of submicron-sized Cr-rich phases, the acid-resistant submicron-sized Cr-rich phases in the CI chondrites are characterized by the depletion of ^{53}Cr and enrichment of ^{54}Cr (Trinquier et al. 2008; Petitat et al. 2011). Therefore, it is difficult to explain the first model, in which dust with an extremely high $\varepsilon^{53}Cr$ value was included in C0027.

Meanwhile, the second model is rather more plausible. Although C0027 has a mineral assemblage and a bulk chemical composition that is not significantly different from that of the other Ryugu particles, it differs from the others in that it contains a significantly higher abundance of phyllosilicate nodules, e.g., 21 vol.% for C0027 and 0–8 vol.% for the others (Table 2). Most of the phyllosilicate nodules in C0027 represent a dense aggregate of fine-grained phyllosilicate minerals that contain no carbonate and sulfide minerals, and are fringed by Fe-sulfides and Mn–Cr oxides. The phyllosilicate nodules are typically depleted in Sr, Ba, and REEs compared to the matrix phyllosilicates (Nakamura et al. 2022). These observations suggest that the phyllosilicate nodules were affected by a different type/additional stage of the aqueous alteration process, compared to that affected the matrix. The aqueous alteration to which the nodules had been subjected is

thought to have decomposed the carbonate and sulfide minerals, leaching the fluid-soluble elements such as Ba and Sr, some of which have recrystallized as sulfide and oxide fringes. Thus, it is likely that excess ^{53}Cr was formed by the decay of ^{53}Mn in carbonate minerals formed by the first stage of aqueous alteration in the nodules. Subsequent aqueous alteration might have decomposed the carbonate minerals and selectively leached Mn relative to Cr, resulting in a decrease of the Mn/Cr, while ^{53}Cr excess was retained. The extremely high abundance of the phyllosilicate nodules in C0027 could have caused excess ^{53}Cr relative to the Mn–Cr isochrons obtained by other samples. To verify this model more precisely, further studies on the origin and evolution of the dense phyllosilicate nodules in the Ryugu samples are needed.

4.3. Implications

The ^{55}Mn/^{52}Cr and ε^{53}Cr values of carbonaceous chondrites show a broadly positive correlation, with CI chondrites having the highest ε^{53}Cr values (Trinquier et al. 2008; Qin et al. 2010; Göpel et al. 2015; Zhu et al. 2021) (Figure 2(b)). This positive correlation could be essentially due to volatility-controlled Mn/Cr fractionation (i.e., Mn loss) of precursor material in a nebular setting with a negative initial ε^{53}Cr value (Shukolyukov & Lugmair 2006; Trinquier et al. 2008). However, as more data are obtained, the mixing effect of the unequilibrated high Mn/Cr and ε^{53}Cr and low Mn/Cr and ε^{53}Cr components (e.g., chondrules, matrix, CAI, presolar grains, etc.) in chondrites became more pronounced, indicating that the slope has little chronological significance (Zhu et al. 2021). The ε^{53}Cr value of bulk Ryugu can be estimated as 0.47 ± 0.10, using a Mn–Cr isochron with a mean ^{55}Mn/^{52}Cr value, obtained from the Ryugu samples. The bulk Ryugu value is plotted on the extrapolated line of positive correlation exhibited by the carbonaceous chondrites, showing that Ryugu is the highest-end member of the trend (Figure 2(b)).

The ε^{54}Cr value of carbonaceous chondrites is known to have a broad positive correlation with the Δ'^{17}O value (Trinquier et al. 2007), and the Ryugu samples show the highest Δ'^{17}O and ε^{54}Cr values (Figure 6). This correlation suggests that different reservoirs with high and low ^{54}Cr and ^{16}O existed in the region where the progenitor bodies of Ryugu and carbonaceous chondrites formed (Trinquier et al. 2007). The ranges of ε^{54}Cr and Δ'^{17}O values were attributed to different processes: nucleosynthesis by supernova explosions (Nittler et al. 2018) and photochemical reactions by the UV-induced self-shielding effect of CO (Thiemens & Heidenreich 1983; Yurimoto & Kuramoto 2004; Lyons & Young 2005), respectively. The heterogeneity of the aforementioned isotopes among the carbonaceous chondrites could be the result of inherited heterogeneities in the protosolar nebula, thermal processes in the inner protoplanetary disk and subsequent convection, and/or later additions to the protoplanetary disk (van Kooten et al. 2016; Burkhardt et al. 2019). It is beyond the scope of this paper to discuss which model is correct, but it is certain that the precursor materials that formed the Ryugu progenitor body must have been rich in the least thermally processed materials, namely, presolar chromium oxide grains (Dauphas et al. 2010; Qin et al. 2010) and H_2O-ice (Clayton 1993), the main reservoirs of the ^{54}Cr-rich and ^{16}O-poor components, respectively. The highest Mn/Cr ratios for Ryugu relative to all carbonaceous chondrites also support this model. The aforementioned evidence suggests that the progenitor body of Ryugu could have formed within the farthermost region of the protoplanetary disk relative to the progenitor bodies of carbonaceous chondrites including CI. However, it should be noted that the Δ'^{17}O values of CI chondrites may have been modified by terrestrial contamination, and slight differences in Δ'^{17}O values between Ryugu and CI chondrites cannot be strictly discussed (Nakamura et al. 2022; Yokoyama et al. 2023a).

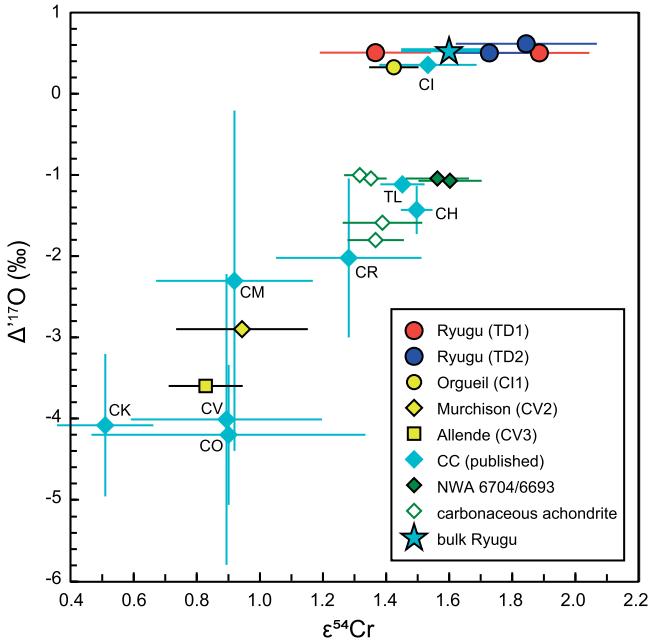

Figure 6. The Δ'^{17}O vs. ε^{54}Cr of Ryugu and carbonaceous meteorites. Data for the ε^{54}Cr are the same as in Figure 3 and Bogdanovski & Lugmair (2004). The carbonaceous achondrites are NWA 7680, NWA 6962, Tafassasset, and NWA 011. Data for Δ'^{17}O are from references (Clayton & Mayeda 1999; Brown et al. 2000; Greenwood & Franchi 2004; Russell et al. 2010; Harju et al. 2014; Schrader et al. 2014; Hibiya et al. 2019; Sanborn et al. 2019; Zhu et al. 2021). TL is Tagish Lake C2-ungrouped chondrite.

Despite accreting at different distances from the Sun, the hydrous asteroids (Ryugu, CI, CM, CR, and ungrouped C2 chondrites) underwent aqueous alteration during the limited duration of 3.8 ± 1.8 Myr after CAI (Figure 1). In addition to these hydrous asteroids, partially or fully melted carbonaceous achondrite progenitor bodies are known to have formed in the outer region of the protoplanetary disk (Hibiya et al. 2019; Sanborn et al. 2019). The ε^{54}Cr value of most of the carbonaceous achondrites ranges between 1.3 and 1.4, the same value as CR chondrites (Bogdanovski & Lugmair 2004; Göpel et al. 2015; Sanborn et al. 2018; Hyde et al. 2022) (Figure 3). However, the paired NWA 6704 and NWA 6693 have a higher ε^{54}Cr value of 1.6 (Sanborn et al. 2019), which is within the range of Ryugu and CI (Figure 6). The initial ε^{53}Cr value of the NWA 6704/6693, obtained from Mn–Cr isochrons using isolated minerals and whole rock was 0.14 ± 0.03 (Sanborn et al. 2019), which is also identical to the value obtained from Ryugu particles but higher than that of CI chondrites, estimated by the bulk ε^{53}Cr value of CI chondrites and their mean aqueous alteration age (4.0 Myr after CAI, mean of CI chondrites in Figure 1). These coincidences between Ryugu and NWA 6704/6693 indicate that the precursors that formed them were formed in close proximity to precursor material that had experienced the same degree of thermal processing.

Meanwhile, the crystallization age of NWA 6704/6693 measured by three chronological methods (Al-Mg, Mn–Cr, and Pb–Pb) is within the error of the aqueous alteration age of Ryugu (Figure 1). The Ryugu progenitor body was heated to <100 °C, whereas NWA 6704/6693 to above the liquidus temperature (Hibiya et al. 2019), and this difference was mainly caused by the distinct accretion ages: a few million years and <∼0.6 Myr after the CAI, respectively (Neumann et al. 2023). The δ^{18}O and Δ'^{17}O values of NWA 6704 were 4.6 and −1.05‰, respectively, which are significantly lower than those of Ryugu (Hibiya et al. 2019; Nakamura et al. 2022). If a similar proportion of ^{16}O-depleted ice and ^{16}O-enriched dust was accreted to form the progenitor body of NWA 6704/6693 and that of Ryugu, the aqueous alteration that occurred during progressive heating of the NWA 6704/6693 progenitor body would cause the Δ'^{17}O value to be comparable to Ryugu, and the subsequent fractionation during the dehydration and vaporization from the body would cause the δ^{18}O value to increase, while the Δ'^{17}O value would remain nearly constant (Clayton & Mayeda 2009). This implies that over the course of a few million years after the formation of CAI, the ice/dust ratio increased in the outer region of the protoplanetary disk, where the progenitor bodies of Ryugu and NWA 6704/6693 were accreted. This might be related to the inward migration of snowline in the protoplanetary disk during this period (e.g., Zhang & Jin 2015; Xiao et al. 2017).

5. Conclusions

The Mn–Cr isotopic systematics of the bulk Ryugu particles provides valuable insights into the formation and aqueous alteration history of the outer solar system. A wide range of Mn/Cr was observed among the samples measured in this study, due to the heterogeneous distribution of carbonate minerals formed by aqueous alteration. The aqueous alteration age of Ryugu particles determined by the Mn–Cr method yielded an age of 4.13 +0.62/−0.55 Myr after the formation of CAI, corresponding to 4563.17 +0.60/−0.67 Myr ago.

One particle (C0027), which exhibits an anomalously high ε^{53}Cr value, causing it to deviate from the isochron, contains an extremely high amount of dense phyllosilicate nodules (21 vol. %). These nodules are thought to be domains that have undergone multiple phases of aqueous alteration. The high ε^{53}Cr value of C0027 may have resulted from this multistep aqueous alteration process.

The unique characteristics of the Ryugu particles, including the highest Mn/Cr, initial ε^{53}Cr, ε^{54}Cr, and Δ'^{17}O values, suggest minimal thermal processing of its precursor materials compared to those in carbonaceous chondrites. Comparisons with carbonaceous achondrites like NWA 6704/6693 indicate the existence of large variations in ice/dust ratios in the outer protoplanetary disk over a few million years after CAI formation.

Acknowledgments

This work was carried out at the JAXA's Hayabusa2 Phase-2 curation facility at the Pheasant Memorial Laboratory, Institute for Planetary Materials, Okayama University. We thank the referees for the suggestions, which have improved the manuscript. The authors are grateful to K. Tanaka for the technical help. This study was supported by the Program for Promoting the Enhancement of Research University by MEXT, by JSPS KAKENHI grants (20K04108, 23K17707), and by JST SPRING grant (JPMJSP2126).

ORCID iDs

Ryoji Tanaka https://orcid.org/0000-0002-7537-255X
Dilan M. Ratnayake https://orcid.org/0000-0001-8373-0479
Tsutomu Ota https://orcid.org/0000-0003-4801-1609
Noah Miklusicak https://orcid.org/0000-0003-1829-3393
Tak Kunihiro https://orcid.org/0000-0001-5605-1227
Christian Potiszil https://orcid.org/0000-0001-9420-4220
Chie Sakaguchi https://orcid.org/0000-0003-0817-0365
Katsura Kobayashi https://orcid.org/0000-0002-1696-1418
Hiroshi Kitagawa https://orcid.org/0000-0002-6492-4208
Masahiro Yamanaka https://orcid.org/0000-0002-7414-3616
Masanao Abe https://orcid.org/0000-0003-4780-800X
Akiko Miyazaki https://orcid.org/0000-0001-7427-2285
Satoru Nakazawa https://orcid.org/0000-0003-4250-1826
Tatsuaki Okada https://orcid.org/0000-0001-6381-8107
Takanao Saiki https://orcid.org/0000-0003-3100-420X
Satoshi Tanaka https://orcid.org/0000-0002-4874-0417
Tomohiro Usui https://orcid.org/0000-0002-4653-293X
Sei-ichiro Watanabe https://orcid.org/0000-0002-5820-2102
Toru Yada https://orcid.org/0000-0002-7971-510X
Kasumi Yogata https://orcid.org/0000-0002-3717-9185
Makoto Yoshikawa https://orcid.org/0000-0002-3118-7475
Eizo Nakamura https://orcid.org/0000-0003-4399-9443

References

Amelin, Y., Koefoed, P., Iizuka, T., et al. 2019, GeCoA, 245, 628
Birck, J.-L., & Allègre, C. J. 1985, GeoRL, 12, 745
Bischoff, A., Alexander, C. M. O. D., Barrat, J.-A., et al. 2021, GeCoA, 293, 142
Bogdanovski, O., & Lugmair, G. W. 2004, LPSC, 35, 1715
Bourdon, B., & Fitoussi, C. 2020, ESC, 4, 1408
Brennecka, G. A., & Wadhwa, M. 2012, PNAS, 109, 9299
Brown, P. G., Hildebrand, A. R., Zolensky, M. E., et al. 2000, Sci, 290, 320
Burkhardt, C., Dauphas, N., Hans, U., et al. 2019, GeCoA, 261, 145
Clayton, R. N. 1993, AREPS, 21, 115
Clayton, R. N., & Mayeda, T. K. 1999, GeCoA, 63, 2089
Clayton, R. N., & Mayeda, T. K. 2009, JPCA, 113, 2212
Connelly, J. N., Bizzarro, M., Krot, A. N., et al. 2012, Sci, 338, 651
Dauphas, N., Remusat, L., Chen, J. H., et al. 2010, ApJ, 720, 1577
Endress, M., Zinner, E., & Bischoff, A. 1996, Natur, 379, 701
Fujiya, W., Sugiura, N., Hotta, H., et al. 2012, NatCo, 3, 627
Fujiya, W., Sugiura, N., Sano, Y., et al. 2013, E&PSL, 362, 130
Göpel, C., Birck, J.-L., Galy, A., et al. 2015, GeCoA, 156, 1
Greenwood, R. C., & Franchi, I. A. 2004, M&PS, 39, 1823
Greenwood, R. C., Franchi, I. A., Findlay, R., et al. 2022, NatAs, 7, 29
Harju, E. R., Rubin, A. E., Ahn, I., et al. 2014, GeCoA, 139, 267
Hibiya, Y., Archer, G. J., Tanaka, R., et al. 2019, GeCoA, 245, 597
Honda, M., & Imamura, M. 1971, PhRvC, 4, 1182
Hyde, B. C., Moser, D. E., Tait, K. T., et al. 2022, M&PS, 57, 1722
Ito, M., Tomioka, N., Uesugi, M., et al. 2022, NatAs, 6, 1163
Jilly-Rehak, C. E., Huss, G. R., & Nagashima, K. 2017, GeCoA, 201, 224
Kadlag, Y., Becker, H., & Harbott, A. 2019, M&PS, 54, 2116
Kawasaki, N., Nagashima, K., Sakamoto, N., et al. 2022, SciA, 8, eade2067
Liu, M.-C., McCain, K. A., Matsuda, N., et al. 2022, NatAs, 6, 1172
Lyons, J. R., & Young, E. D. 2005, Natur, 435, 317
Makishima, A., Yamakawa, A., Yamashita, K., et al. 2010, ChGeo, 274, 82
McCain, K. A., Matsuda, N., Liu, M.-C., et al. 2023, NatAs, 7, 309
Nakamura, E., Kobayashi, K., Tanaka, R., et al. 2022, PJAB, 98, 227
Nakamura, T., Matsumoto, M., Amano, K., et al. 2023, Sci, 379, eabn8671
Nakashima, D., Nakamura, T., Zhang, M., et al. 2023, NatCo, 14, 532
Nakato, A., Inada, S., Furuya, S., et al. 2022, GeocJ, 56, 197
Neumann, W., Ma, N., Bouvier, A., et al. 2023, arXiv:2302.13303

Nittler, L. R., Alexander, C. M. O. D., Liu, N., et al. 2018, ApJL, 856, L24
Petitat, M., Birck, J. L., Luu, T. H., et al. 2011, ApJ, 736, 23
Potiszil, C., Ota, T., Yamanaka, M., et al. 2023, NatCo, 14, 1482
Qin, L., Alexander, C. M. O. D., Carlson, R. W., et al. 2010, GeCoA, 74, 1122
Ratnayake, D. M., Tanaka, R., & Nakamura, E. 2023, AcAC, 1278, 341723
Russell, S. D. J., Longstaffe, F. J., King, P. L., et al. 2010, GeCoA, 74, 2484
Sanborn, M. E., Wimpenny, J., Williams, C. D., et al. 2019, GeCoA, 245, 577
Sanborn, M. E., Yin, Q.-Z., Hyde, B. C., et al. 2018, LPSC, 49, 2296
Schrader, D. L., Nagashima, K., Krot, A. N., et al. 2014, GeCoA, 132, 50
Shukolyukov, A., & Lugmair, G. W. 2006, E&PSL, 250, 200
Spandler, C., & O'Neill, H. S. C. 2010, CoMP, 159, 791
Sugita, S., Honda, R., Morota, T., et al. 2019, Sci, 364, eaaw0422
Tachibana, S., Sawada, H., Okazaki, R., et al. 2022, Sci, 375, 1011
Thiemens, M. H., & Heidenreich, J. E. 1983, Sci, 219, 1073
Trinquier, A., Birck, J.-L., & Allègre, C. J. 2007, ApJ, 655, 1179
Trinquier, A., Birck, J. L., Allegre, C. J., et al. 2008, GeCoA, 72, 5146
van Kooten, E. M. M. E., Wielandt, D., Schiller, M., et al. 2016, PNAS, 113, 2011
Vermeesch, P. 2018, GeoFr, 9, 1479
Visser, R., John, T., Whitehouse, M. J., et al. 2020, E&PSL, 547, 116440
Watanabe, S., Hirabayashi, M., Hirata, N., et al. 2019, Sci, 364, 268
Xiao, L., Niu, R., & Zhang, H. 2017, MNRAS, 467, 2869
Yada, T., Abe, M., Okada, T., et al. 2021, NatAs, 6, 214
Yamakawa, A., Yamashita, K., Makishima, A., et al. 2009, AnaCh, 81, 9787
Yokoyama, T., Nagashima, K., Nakai, I., et al. 2023a, Sci, 379, eabn7850
Yokoyama, T., Ohkuma, Y., Nishikawa, K., et al. 2023b, GGRes, 47, 415
Yokoyama, T., Wadhwa, M., Iizuka, T., et al. 2023c, SciA, 9, eadi7048
Yurimoto, H., & Kuramoto, K. 2004, Sci, 305, 1763
Zhang, Y., & Jin, L. 2015, ApJ, 802, 58
Zhu, K., Moynier, F., Schiller, M., et al. 2021, GeCoA, 301, 158